Hydrogen and NH$_3$ co-adsorption on Pd–Ag membranes

Didrik R. Småbråten [a],[*], Marie D. Strømsheim [b], Thijs Peters [a]

[a] Department of Sustainable Energy Technology, SINTEF Industry, PO Box 124 Blindern, NO-0314 Oslo, Norway
[b] Hydrogen Mem-Tech AS, Leirfossvegen 27 A, NO-7038 Trondheim, Norway

A B S T R A C T

Ammonia (NH$_3$) represents a carbon-free hydrogen carrier that can be used as a zero-emission fuel in the maritime and heavy transport sector with hydrogen fuel cells. To use ammonia as feedstock, the hydrogen must be recovered through NH$_3$ decomposition into H$_2$ and N$_2$. Ammonia decomposition by a membrane-enhanced reactor would inherently produce high-purity H$_2$ through the membrane avoiding the need for a costly hydrogen separation/purification unit. Pd-based membrane reactors can obtain full ammonia decomposition and show significantly higher conversion than conventional reactors. However, the H$_2$ permeability is found to be inhibited in the presence of NH$_3$. A further fundamental understanding of the long-term stability and performance of the Pd-based membranes under exposure to NH$_3$ is therefore required. In the current work, the adsorbate-adsorbate interactions during co-adsorption, the influence the presence of NH$_3$ has on the hydrogen dissociation kinetics, and surface segregation effects in the presence of NH$_3$ and/or hydrogen on the surface of Pd and Pd$_3$Ag are investigated in detail using density functional theory calculations. We find that both the hydrogen surface coverage and dissociation kinetics are hindered by the presence of NH$_3$ on the surface, and possible segregation of Ag towards the surface in the presence of NH$_3$, which could explain the reduced hydrogen permeation in NH$_3$.

1. Introduction

Ammonia (NH$_3$) is a particularly promising hydrogen carrier due to its high volumetric energy density, relatively low cost and ease of liquefaction, storage, and transportation [1]. Ammonia is produced in large quantities world-wide and safe handling of this toxic product is commonly established. NH$_3$ represents a carbon-free alternative and can be used as a zero-emission fuel in the maritime and heavy transport sector, either through the use of ammonia combustion engines [2–4] or fuel cells, i.e. solid oxide fuel cells (SOFCs) or polymer electrolyte membranes fuel cells (PEM-FCs) [5–8]. To use ammonia as fuel for SOFCs or PEM-FCs, the hydrogen has firstly to be recovered through NH$_3$ decomposition into H$_2$ and N$_2$. According to the Le Chatelier's principle, the NH$_3$ decomposition reaction is favored at low pressures, and due its endothermic nature, by high temperatures. Conventionally, a NH$_3$ decomposition reactor operating at relatively high temperatures for near complete conversion, combined with a separation system to separate H$_2$ from N$_2$ and trace amounts of unconverted NH$_3$, is applied. Halseid investigated the effect of ammonia on polymer electrolyte PEM-FCs, and showed that even the addition of 1 ppm NH$_3$ to the hydrogen feed resulted in significant performance loss [9].

A membrane-enhanced reactor technology has been considered as a promising system to efficiently recover the H$_2$ stored in NH$_3$ [10–16]. The use of a membrane reactor for ammonia decomposition would inherently produce high-purity H$_2$ through the membranes, avoiding the

need for a costly hydrogen separation/purification unit [11,13,14, 17–19]. Also, the thermodynamic equilibrium is shifted, and because it is possible to obtain full ammonia conversion the need for downstream cleaning of unconverted ammonia is reduced. For example, García-García et al. [10] could achieve 100% ammonia decomposition at 635 K with a 40 μm stainless steel supported tubular Pd-membrane in combination with a Ru-based catalyst, compared to 65% for a thermodynamically limited conventional reactor without hydrogen extraction. Similarly, Collins et al. [11] demonstrated an increase in the ammonia conversion at 873 K from 53% for a conventional reactor to over 94% with a Pd-based membrane reactor employing a composite palladium membrane with selective layer thickness of 11.4 μm. They also found that the equilibrium shift was even higher at lower temperatures, with an increase in the ammonia conversion from 17% to 79% at 823 K with the conventional and membrane reactors, respectively. Along the same line, Itoh et al. [12] obtained a 60% hydrogen recovery and a 15% increase in conversion compared to a conventional packed reactor by employing a membrane reactor with a 200 μm-thick palladium tube at 723 K. Also Zhang et al. [15] investigated the membrane-integrated ammonia decomposition process. However, a sequential system of an NH$_3$ decomposition reactor followed by Pd membrane separator for H$_2$ purification was proposed because it was observed that the membrane performance was greatly limited by its low effective utilization in the NH$_3$-rich zone. In their sequential process a H$_2$ flux and purity of 54 m^3 m^{-2} h^{-1} and 99.96% were obtained, respectively, at a H$_2$ recovery of

---

* Corresponding author.
  E-mail address: didrik.smaabraaten@sintef.no (D.R. Småbråten).

77%. Throughout a 500-h lifetime test, both the decomposition and separation units showed good stability, although residual NH_3 in the gaseous stream towards the purification unit slightly inhibited the permeability of the Pd membrane [15].

In a previous study [16] we also experimentally demonstrated a substantial H_2 flux inhibition during long-term performance testing of a PdAg membrane under relatively low concentrations of NH_3 ranging from 10 to 500 ppm at lower temperatures between 300 and 450 °C . In the same work, density functional theory (DFT) calculations were used to evaluate possible blocking of the membrane surface through competitive adsorption between H and NH_3 related species [16]. The calculations showed no significant reduction in the hydrogen surface coverage under experimentally relevant operating conditions. This is in contrast to the study on competitive adsorption of H and S by Peters et al. [20], where they calculated a lowering of the hydrogen surface coverage by 79–56% with 25–75 ppb H_2S at 673 K comparable to the experimentally measured reduction in the H_2 flux of 91–77%. Hence, our previous work [16] concluded that the observed H_2 flux inhibition during exposure to NH_3 could not be explained by competitive adsorption. Other possible explanations were suggested, such as changes in the kinetics of hydrogen dissociation and incorporation, or microstructural changes upon exposure to NH_3, however these were not further studied in Ref. [16]. While single adsorption of NH_x ($x = 1$–3) species, co-adsorption of hydrogen and NH_x ($x = 0$–2) species, and dehydrogenation of NH_3 on Pd(111) have previously been studied using DFT calculations [21–24], co-adsorption of NH_3 and hydrogen and how the presence of NH_3 affect the hydrogen dissociation kinetics and surface composition for PdAg surfaces have not been studied in detail. Such phenomena have, however, been studied computationally for co-adsorption of H and CO on PdAg surfaces [25,26]. Svenum et al. [25] found that CO pre-adsorbed on the surface significantly weakens the hydrogen adsorption. Furthermore, they demonstrated a significant increase in the energy barrier for H_2 dissociation with increasing CO coverage. In another study, Svenum et al. [14] showed that Pd segregates towards the surface of Pd_3Ag(111) for large H and CO surface coverages.

Building on the previous knowledge on competitive adsorption of H and NH_3 and co-adsorption of H and CO on Pd(111) and Pd_3Ag(111) surfaces [16,25,26], we investigate in the current work adsorbate-adsorbate interactions during co-adsorption of H and NH_3, the influence the presence of NH_3 has on the hydrogen dissociation kinetics, and surface segregation effects in the presence of NH_3 and/or H using DFT calculations. Compared to our previous work [16], higher ammonia levels, and thus coverages relevant for a membrane-integrated ammonia decomposition reactor, have also been considered. We find that both the hydrogen surface coverage and dissociation kinetics are hindered by the presence of NH_3 on the surface at higher ammonia levels and surface coverages. Furthermore, our calculations indicate possible segregation of Ag towards the surface in the presence of NH_3. This could explain the measured long-term H_2 flux inhibition in NH_3.

2. Methods

The DFT calculations were performed using the projector augmented wave (PAW) method as implemented in VASP [27–29], using the GGA-PBE [30] functional. The calculations were carried out with a plane-wave cutoff energy of 500 eV and an electronic convergence criterion of 10^{-6} eV. Pd (5s, 4d), Ag (5s, 4d), H (1s), and N (2s, 2p) were treated as valence electrons. The (111) surfaces were modelled by 7 atomic layer slabs. The periodic images were separated by a vacuum region of 25 Å, including dipole corrections. Surface coverages were calculated as the number of adsorbed molecules per surface metal atom, where one monolayer ($\theta = 1$) corresponds to one adsorbed atom or molecule per surface metal atom. The majority of the calculations were performed using $p(2 \times 2)$ supercells (4 surface metal atoms), except for surface coverages $\theta = 1/16$ where $p(4 \times 4)$ supercells (16 surface metal

atoms) were used. Atomic positions were relaxed until the residual forces were below 0.02 eV Å^{-1}, where the two bottom layers were fixed to bulk positions. The adsorbates were further relaxed to a force criterion of 10^{-4} eV Å^{-1} when calculating the vibrational frequencies. A Γ-centered $6 \times 6 \times 1$ k-point grid was used for the $p(2 \times 2)$ slabs, and $3 \times 3 \times 1$ for the $p(4 \times 4)$ slabs. The energy barriers for H_2 dissociation were calculated using the climbing-image nudged elastic band (cNEB) method [31,32], using 11 intermediate images. Each image was relaxed until the residual forces were below 0.02 eV Å^{-1}. Surface segregation as a function of surface coverage for different adsorbates was determined from calculated relative energies for seven different surface configurations as described in Ref. [26].

The equilibrium thermodynamics at finite temperature were assessed through calculated Gibbs adsorption energies of the reactions in Eqs. (1)–(5) according to

$$\Delta G^{ads} = \Delta H^{ads} - T\Delta S^{ads} \tag{1}$$

where ΔH^{ads} and ΔS^{ads} are the adsorption enthalpies and entropies, respectively. The adsorption enthalpies were calculated by

$$\Delta H^{ads} = \Delta E_{DFT}^{ads} - \left(E_{DFT}^{gas} + H_{ref}^{gas} \right) + \Delta ZPE \tag{2}$$

where ΔE_{DFT}^{ads} is the DFT calculated total energy differences for the slabs with and without adsorbed species, E_{DFT}^{gas} the DFT calculated total energy of gaseous H_2 or NH_3, and H_{ref}^{gas} the reference states for the gaseous species at finite temperatures taken from thermochemical data [33]. The zero-point energy (ZPE) contributions were calculated from the normal mode frequencies ν_i by the finite displacement method according to

$$ZPE = \sum_i \frac{h\nu_i}{2} \tag{3}$$

The adsorption entropy of NH_3 was obtained from the empirical relations by Campbell and Sellers [34], while the adsorption entropy of the other species were calculated by

$$\Delta S^{ads}(T) = S_{vib}^{ads}(T) - S_{ref}^{gas}(T) \tag{4}$$

Here, S_{ref}^{gas} is the absolute entropy of the gas molecules taken from thermochemical data [33], and S_{vib}^{ads} is the vibrational entropy of the adsorbed atoms or molecules calculated from the normal mode frequencies ν_i by the finite displacement method according to

$$S_{vib}^{ads} = k \sum_i \left(\frac{\beta_i}{\exp(\beta_i) - 1} - \ln(1 - \exp(-\beta_i)) \right) \tag{5}$$

where $\beta_i = h\nu_i/k_BT$

3. Results

3.1. Thermodynamic model

First, the thermodynamics for competitive adsorption of hydrogen and NH_3 related species reported in Ref. [16] are revisited with larger ammonia levels. Three surfaces are investigated; Pd(111) for reference, Pd_3Ag-terminated Pd_3Ag(111), and Pd-terminated Pd_3Ag(111).

The adsorption thermodynamics for the hydrogen and NH_3 related species were evaluated by the following reactions [16]:

$$\frac{1}{2}H_2(g) + * \rightleftharpoons *H \tag{6}$$

$$NH_3(g) + * \rightleftharpoons *N + \frac{3}{2}H_2(g) \tag{7}$$

$$NH_3(g) + * \rightleftharpoons *NH + H_2(g) \tag{8}$$

$$NH_3(g) + * \rightleftharpoons *NH_2 + \frac{1}{2}H_2(g) \tag{9}$$

$$NH_3(g) + * \rightleftharpoons *NH_3 \tag{10}$$

where * denotes a surface site or an adsorbed atom or molecule on the surface. To minimize any adsorbate-adsorbate interactions, the thermodynamic properties were calculated for surface coverages of $\theta_i = 1/16$. Table 1 shows a summary of the calculated adsorption enthalpies, entropies, Gibbs energies, and vibrational frequencies for the lowest-energy adsorption configurations for the different species at 673 K (typical operating temperatures) and $\theta_i = 1/16$. The resulting structures of the adsorbed species on the Pd-terminated Pd$_3$Ag(111) surface are shown in Fig. 1(b)-(f).

Hydrogen and NH$_3$ show strong adsorption energies in the range of, respectively, −0.30 to −0.24 eV and −0.42 to −0.27 eV, where NH$_3$ shows the strongest adsorption, in agreement with previous reports [16, 21]. Oppositely, N, NH and NH$_2$ show positive adsorption energies, where N is the most unstable adsorbate with adsorption energies of 1.13–1.43 eV.

The adsorption thermodynamics can be further explained by the changes in local electronic density of states (DOS) upon adsorption shown in Fig. 2. The chemical bonding between the adsorbates and the surface Pd-atoms become apparent by the emerging overlapping bonding states between Pd and H or N at the bottom of the valence band. The adsorption of N and NH results in the emergence of empty N-states above the Fermi-level, and significantly lower density for the Pd states at Fermi-level. From previous work on palladium hydrides [35], the latter is known to destabilizes the system, which could explain the positive adsorption enthalpies for N and NH. Oppositely, H and NH$_3$ give no significant changes in the local Pd DOS at the Fermi-level, and hence no destabilization effects upon adsorption. Adsorption of NH$_2$ shows an intermediate change in the local DOS compared to the other compounds, in agreement with the adsorption enthalpies.

The equilibrium surface coverages θ_i can be expressed by the equilibrium constant of the reactions in Eqs. (6)–(10) according to:

$$K_1 = \theta_H \theta_v^{-1} p_{H_2}^{-1/2} = \exp\left(-\frac{\Delta H_1^{ads}}{kT}\right)\exp\left(\frac{\Delta S_1^{ads}}{k}\right) = \exp\left(-\frac{\Delta G_1^{ads}}{kT}\right) \tag{11}$$

Table 1
Calculated adsorption thermodynamics for hydrogen and NH$_3$ related species according to the reactions in Eqs. (6)–(10) at T = 673 K and with $\theta_i = 1/16$.

Species	Site	ΔH_i^{ads} (eV)	$T\Delta S_i^{ads}$ (eV)	ΔG_i^{ads} (eV)	ν_i (cm^{-1})
Pd(111)					
*H	fcc(Pd)	−0.70	−0.45	−0.25	945, 852, 851
*N	fcc(Pd)	1.34	0.21	1.13	514, 513, 463
*NH	fcc(Pd)	0.51	−0.25	0.75	3369, 747, 746, 476, 452, 452
*NH$_2$	bridge (Pd)	−0.03	−0.64	0.60	3480, 3382, 1463, 707, 648, 596, 444, 337, 162
*NH$_3$	top(Pd)	−1.08	−0.66	−0.41	–
Pd$_3$Ag-terminated Pd$_3$Ag(111)					
*H	fcc(Ag)	−0.69	−0.45	−0.24	911, 900, 900
*N	fcc(Ag)	1.64	0.21	1.43	512, 512, 453
*NH	fcc(Ag)	0.87	−0.24	1.11	3349, 752, 746, 454, 451, 439
*NH$_2$	bridge (Pd)	0.17	−0.63	0.80	3476, 3385, 1473, 689, 634, 582, 417, 312, 168
*NH$_3$	top(Pd)	−0.94	−0.66	−0.27	–
Pd-terminated Pd$_3$Ag(111)					
*H	fcc(Pd)	−0.75	−0.45	−0.30	931, 885, 845
*N	fcc(Pd)	1.34	0.21	1.13	525, 513, 442
*NH	fcc(Pd)	0.53	−0.24	0.77	3360, 735, 724, 459, 445, 439
*NH$_2$	bridge (Pd)	−0.03	−0.63	0.60	3470, 3376, 1462, 717, 647, 581, 432, 341, 154
*NH$_3$	top(Pd)	−1.08	−0.66	−0.42	–

$$K_2 = \theta_N \theta_v^{-1} p_{NH_3}^{-1} p_{H_2}^{3/2} = \exp\left(-\frac{\Delta H_2^{ads}}{kT}\right)\exp\left(\frac{\Delta S_2^{ads}}{k}\right) = \exp\left(-\frac{\Delta G_2^{ads}}{kT}\right) \tag{12}$$

$$K_3 = \theta_{NH} \theta_v^{-1} p_{NH_3}^{-1} p_{H_2} = \exp\left(-\frac{\Delta H_3^{ads}}{kT}\right)\exp\left(\frac{\Delta S_3^{ads}}{k}\right) = \exp\left(-\frac{\Delta G_3^{ads}}{kT}\right) \tag{13}$$

$$K_4 = \theta_{NH_2} \theta_v^{-1} p_{NH_3}^{-1} p_{H_2}^{1/2} = \exp\left(-\frac{\Delta H_4^{ads}}{kT}\right)\exp\left(\frac{\Delta S_4^{ads}}{k}\right) = \exp\left(-\frac{\Delta G_4^{ads}}{kT}\right) \tag{14}$$

$$K_5 = \theta_{NH_3} \theta_v^{-1} p_{NH_3}^{-1} = \exp\left(-\frac{\Delta H_5^{ads}}{kT}\right)\exp\left(\frac{\Delta S_5^{ads}}{k}\right) = \exp\left(-\frac{\Delta G_5^{ads}}{kT}\right) \tag{15}$$

where θ_v is the concentration of empty surface sites. The equilibrium surface coverages are obtained by solving Eqs. 11–15 while simultaneously conserving the total number of adsorption sites according to

$$\theta_H + \theta_N + \theta_{NH} + \theta_{NH_2} + \theta_{NH_3} + \theta_v = 1 \tag{16}$$

Focusing on the strongly adsorbed species H and NH$_3$, the calculated surface coverages as a function of relative partial pressures p_{NH3}/p_{H2} in the temperature range from 473 K to 723 K are shown in Fig. 3. We find that the H coverage is unaltered for $p_{NH3}/p_{H2} \lesssim 10^{-3}$, in line with our previous results [16]. For $p_{NH3}/p_{H2} \gtrsim 10^{-3}$ the surface coverage of NH$_3$ starts increasing on the expense of the H coverage, indicating competitive adsorption between H and NH$_3$ at higher ammonia levels.

The results in Fig. 3 also show that the favoring of NH$_3$ over H are shifted to lower p_{NH3}/p_{H2} values with decreasing temperature. To further illustrate this, the surface coverages as a function of temperature with constant $p_{H2} = 1$ bar and varying p_{NH3} is shown in Fig. 4. For the Pd-terminated Pd$_3$Ag(111) surface at, e.g., $p_{NH3} = 0.01$ bar (i.e., $p_{NH3}/p_{H2} = 10^{-2}$), θ_H is reduced from 0.94 to 0.75, accompanied by an increase in θ_{NH_3} from 0.05 to 0.25, when the temperature is reduced from 723 to 473 K.

This trend can be reasoned from the changes in adsorption thermodynamic properties for adsorption of hydrogen and NH$_3$ as a function of temperature plotted in Fig. 5. The adsorption Gibbs energy decreases with decreasing temperature as shown in Fig. 5(c,f,i). This stabilization effect with decreasing temperature is mainly governed by the changes in entropy in Fig. 5(b,e,h). The adsorption Gibbs energy of NH$_3$ becomes more negative relative to hydrogen with reducing temperature, as illustrated by the relative difference in blue in Fig. 5(c,f,i). This means that adsorbed NH$_3$ becomes increasingly more stable compared to hydrogen with reducing temperature, which is in line with experimental observations showing that hydrogen flux inhibition becomes more pronounced at lower temperatures [16]. Note that the relative shift of the Pd$_3$Ag-terminated surface to higher p_{NH3}/p_{H2} in Fig. 3(c,d) compared to the Pd-terminated surfaces can be reasoned from the significant weaker NH$_3$ adsorption on the Pd$_3$Ag-terminated surface as shown in Table 1 and Fig. 5.

3.2. Adsorbate-adsorbate interactions

The thermodynamic modelling described above does not take adsorbate-adsorbate interactions into account. Such interactions are expected to become significant with higher surface coverages, especially for larger molecules such as NH$_3$.

Fig. 6(a) shows the adsorption energy of hydrogen as a function of surface coverage θ_H at 673 K. For the two Pd-terminated surfaces, the adsorption energy is negative up to $\theta_H = 1$, suggesting that the initially clean surfaces will be fully saturated by hydrogen. For the Pd$_3$Ag-terminated surface, the adsorption energy becomes positive for $\theta_H = 3/4$, suggesting a saturation coverage of $\theta_{H,sat} = 1/2$ at 673 K. All three surfaces show a saturation coverage of $\theta_{NH3,sat} = 1/4$ at 673 K (Fig. 6
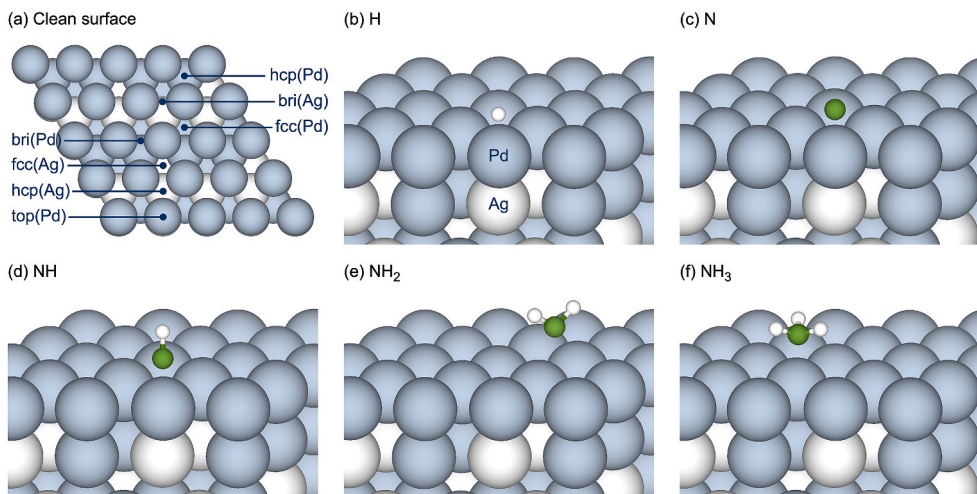
Fig. 1. (a) Most relevant adsorption sites on a Pd-terminated Pd$_3$Ag(111) slab, and relaxed adsorbates of (b) H, (c) N, (d) NH, (e) NH$_2$, and (f) NH$_3$. Only the first three atomic layers are shown in (b)–(f) for clarity.
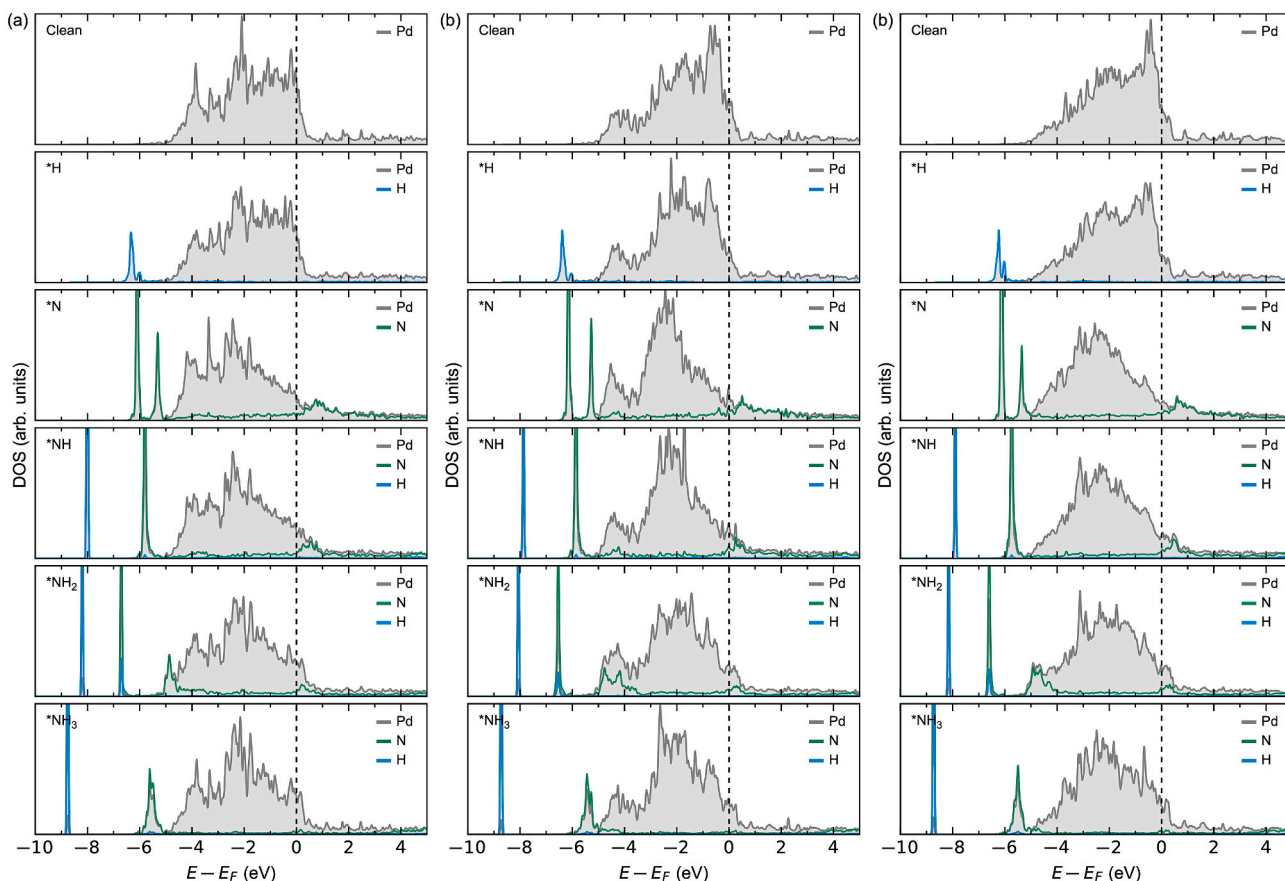

Fig. 2. Atomically resolved electronic density of states (DOS) of the clean surface and with NH$_3$ related adsorbates for (a) Pd(111), (b) Pd$_3$Ag-terminated Pd$_3$Ag (111), and (c) Pd-terminated Pd$_3$Ag(111). The DOS are evaluated for the atoms in the vicinity of the adsorbates and are scaled per atom.

(b)). The dips in the adsorption energy profiles for the Pd$_3$Ag-surfaces at higher coverages in Fig. 6(b) could be due to partial detachment of NH$_3$ from the surface during structural optimization.

Note that the above stated saturation surface coverages θ_{sat} refer to the largest DFT modelled coverage with a negative Gibbs energy (ΔG^{ads} < 0), while a more accurate saturation coverage might lie in-between the discrete modelled ones. This could be addressed by multiple additional DFT model systems, however, for addressing general trends the

explicit results in Fig. 6 should still be valid.

Fig. 7 shows the changes in adsorption energy of hydrogen as a function of hydrogen coverage under the assumption that the surface is pre-adsorbed with $\theta_{NH3} = 1/4$. For all surfaces, a significant destabilization of hydrogen adsorption, in the order of ~0.2 eV, is observed. The corresponding saturation coverages are reduced to $\theta_{H,sat} = 1/2$ for the Pd-terminated surfaces, and $\theta_{H,sat} = 1/4$ for the Pd$_3$Ag-terminated surface.
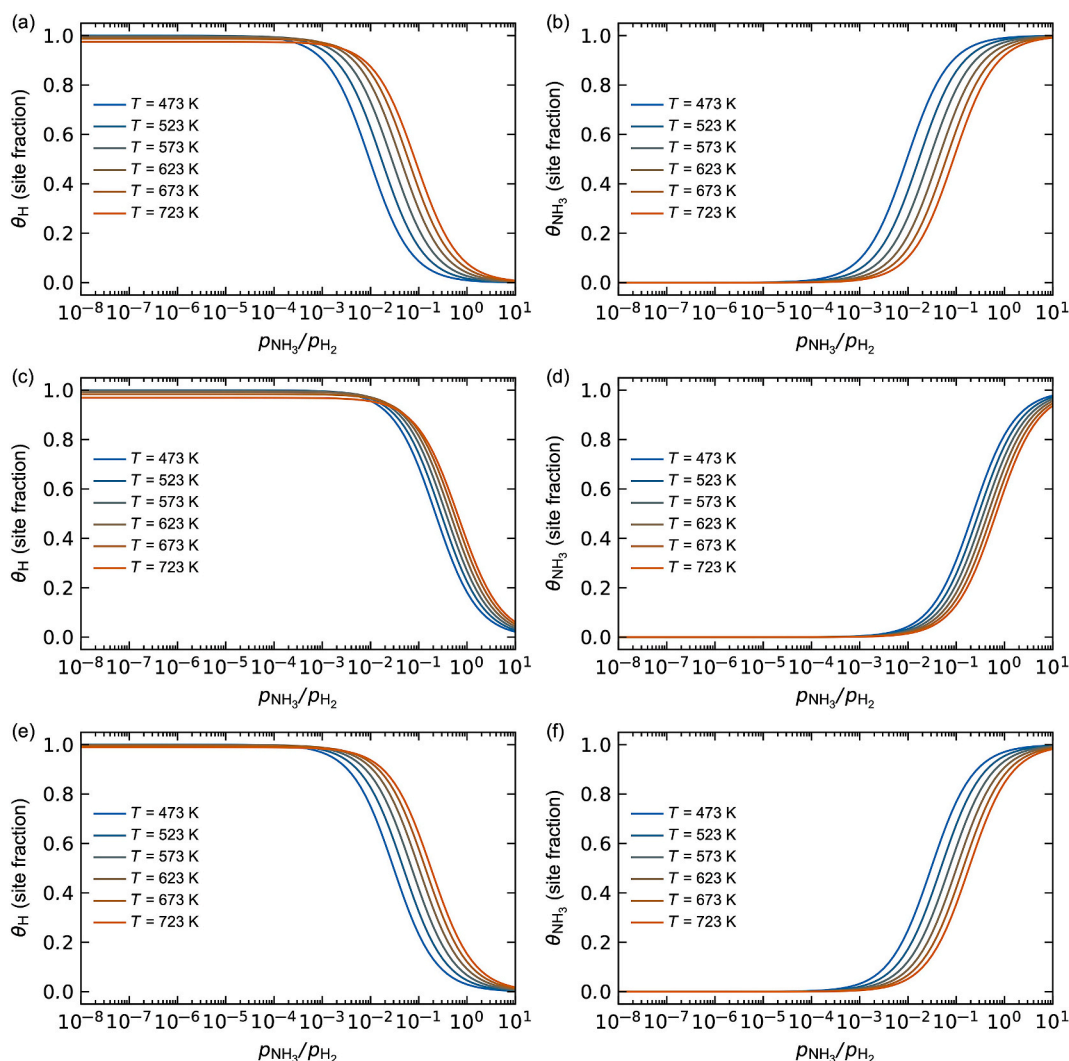
Fig. 3. Calculated equilibrium coverages for (a,c,e) hydrogen and (b,d,f) ammonia on (a,b) Pd(111), (c,d) Pd$_3$Ag-terminated Pd$_3$Ag(111), and (e,f) Pd-terminated Pd$_3$Ag(111) as a function of relative partial pressures of H$_2$ (g) and NH$_3$ (g) at p_{H2} = 1 bar in the temperature range of 473–723 K.

3.3. Hydrogen dissociation kinetics

The H$_2$ flux should also depend on changes in the hydrogen dissociation energetics in the presence of pre-adsorbed molecules, as reported for CO and hydrogen on Pd$_3$Ag(111) [25]. Using the predicted NH$_3$ saturation coverages of θ_{NH3} = 1/4 for all three surfaces from Fig. 6(b), the calculated minimum energy paths (MEP) for the dissociation:

$$H_2(g) + 2* \rightarrow *H + *H \qquad (8)$$

on the $p(2x2)$ surface with and without the presence of NH$_3$ is shown in Fig. 8.

The dissociation is a non-activated process on the clean surfaces [36, 37], as evident from the lack of an energy barrier relative to H$_2$ (g) across the MEP in Fig. 8 (black curves). The dissociation goes through a local energy minimum, corresponding to a metastable physisorbed H$_2$ molecule on a top site, referred to as an "fcc-fcc precursor state" in the literature [36]. The subsequent splitting of the H–H bond to form two H on adjacent fcc-sites comes with a small energy cost of ~0.05 eV, apparent from the local transition state (saddle point) along the MEP. A representative visualization of the calculated initial, precursor, transition, and final states for the hydrogen dissociation on the clean Pd-terminated Pd$_3$Ag (111) surface is shown in Fig. 9(a). Comparable dissociation paths are found for the other surfaces investigated.

We find two possible dissociation paths with NH$_3$ pre-adsorbed on the surface. Dissociation path (1), plotted in blue in Fig. 8, follows a comparable mechanism as for the pristine Pd(111) surface; the dissociation goes through a physisorbed H$_2$-molecule on a top-site adjacent to the pre-adsorbed NH$_3$, and a subsequent splitting of the H–H bond to form two H on two adjacent fcc-sites. Dissociation path (2), plotted in red in Fig. 8, shows a different mechanism; the dissociation goes through a physisorbed H$_2$-molecule on a neighboring bridge-site, before splitting to form two H on two adjacent fcc-sites. We find that path (2) occurs on all three surfaces investigated, while path (1) only occurs for the Pd-rich surfaces. This is because path (1) on the Pd$_3$Ag-terminated Pd$_3$Ag(111) goes through an unstable H$_2$-molecule on a Ag-top site, where ci-NEB calculations initialized according to path (1) relaxes back to path (2) (not shown). The two paths are visualized for the Pd-terminated Pd$_3$Ag (111) surface in Fig. 9(b and c).

With NH$_3$ pre-adsorbed on the surface, the dissociation becomes an activated process, with energy barriers relative to H$_2$ (g) in the order of ~0.2 eV for all three systems. For path (1), the emergence of an energy barrier can be reasoned from steric hindrance of the top-sites in the presence of pre-adsorbed NH$_3$, which results in significant adsorbate-adsorbate interactions and corresponding energy cost during the hydrogen dissociation. The adsorbate-adsorbate interactions are less pronounced for path (2) due to longer adsorbate-adsorbate distances upon physisorption. However, the change in the dissociation mechanism to H$_2$ physisorbed on a bridge-site comes with an additional cost relative
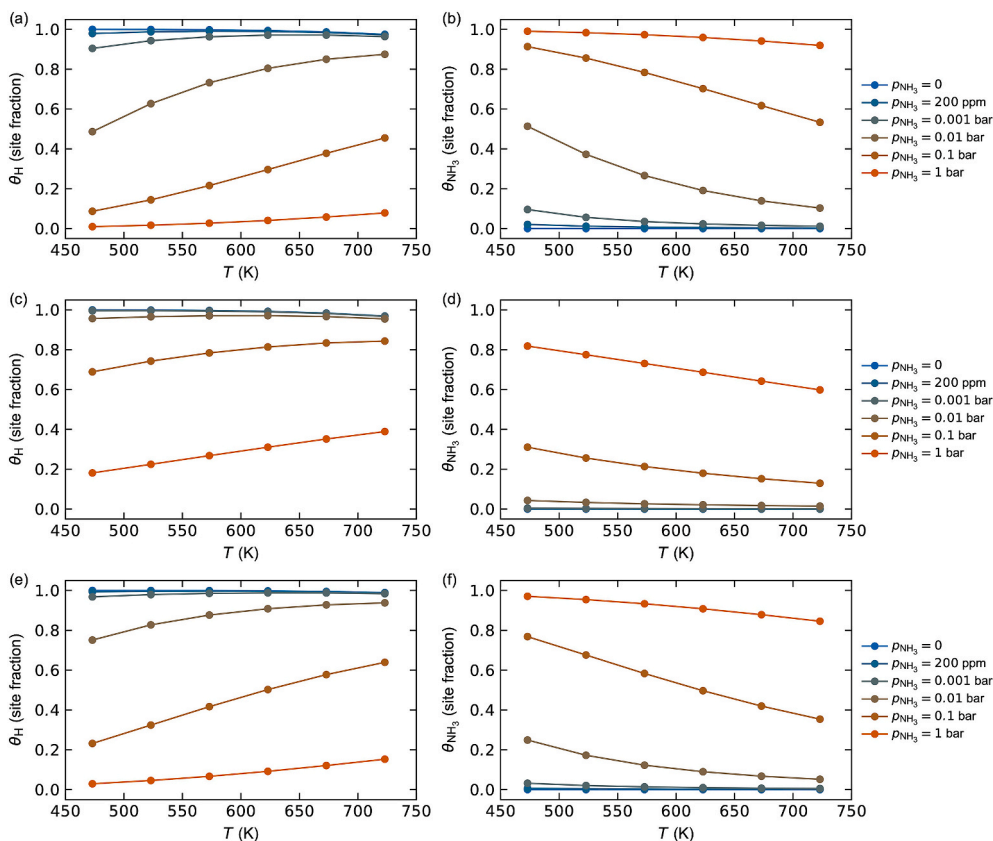
Fig. 4. Calculated equilibrium coverages for (a,c,e) hydrogen and (b,d,f) ammonia on (a,b) Pd(111), (c,d) Pd₃Ag-terminated Pd₃Ag(111), and (e,f) Pd-terminated Pd₃Ag(111) as a function of temperature with varying partial pressure of NH₃ (g) at $p_{H2} = 1$ bar.
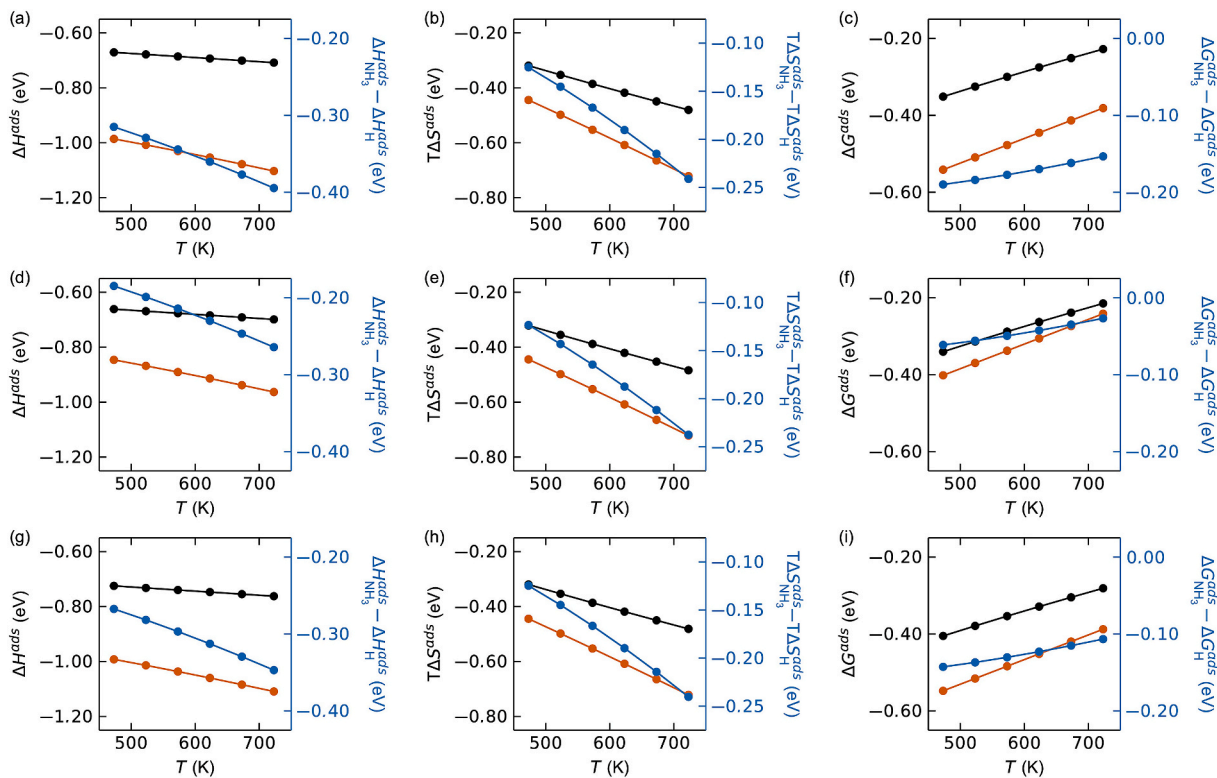

Fig. 5. Calculated (a,d,g) enthalpies, (b,e,h) entropies, (c,f,i) and Gibbs energies for adsorption of hydrogen (black) and NH₃ (red) on (a–c) Pd(111), (d–f) Pd₃Ag-terminated Pd₃Ag(111), and (g–i) Pd-terminated Pd₃Ag(111) as a function of temperature. The difference in thermodynamics between adsorption of hydrogen and NH₃ are plotted in blue. (For interpretation of the references to colour in this figure legend, the reader is referred to the Web version of this article.)
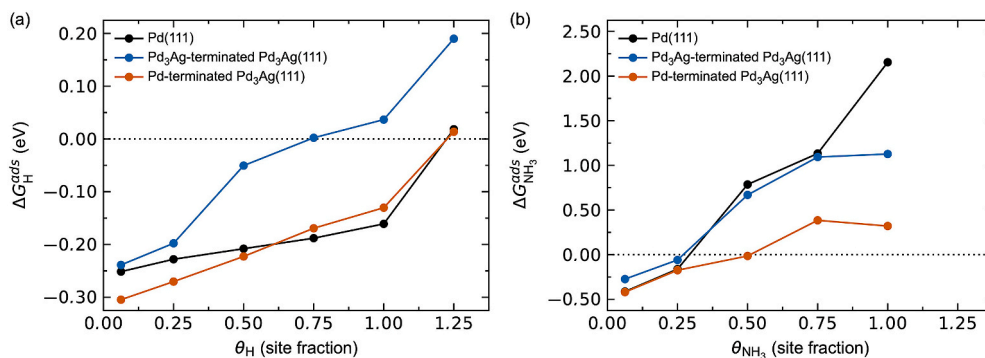
Fig. 6. Calculated adsorption energy at 673 K for (a) hydrogen and (b) NH$_3$ as a function of surface coverage, θ_i, on Pd(111), Pd$_3$Ag-terminated Pd$_3$Ag(111), and Pd-terminated Pd$_3$Ag(111).
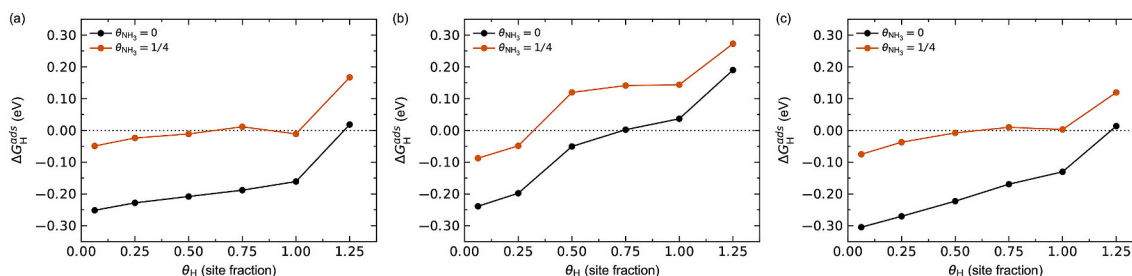

Fig. 7. Calculated hydrogen adsorption energy at 673 K with (red) and without (black) pre-adsorbed NH$_3$ on (a) Pd(111), (b) Pd$_3$Ag-terminated Pd$_3$Ag(111), and (c) Pd-terminated Pd$_3$Ag(111). (For interpretation of the references to colour in this figure legend, the reader is referred to the Web version of this article.)
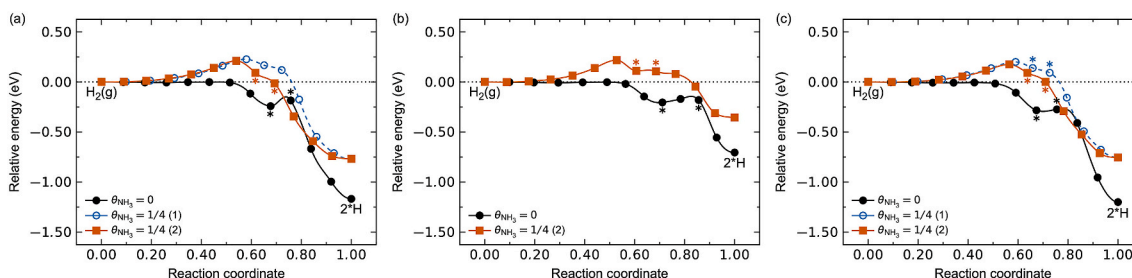

Fig. 8. Calculated MEP for hydrogen dissociation with (red and blue) and without (black) pre-adsorbed NH$_3$ on (a) Pd(111), (b) Pd$_3$Ag-terminated Pd$_3$Ag(111), and (c) Pd-terminated Pd$_3$Ag(111). The asterisks along the MEPs correspond to the precursor state (first) and transition state (second), visualized in Fig. 9. (For interpretation of the references to colour in this figure legend, the reader is referred to the Web version of this article.)

to H$_2$ physisorbed on a top-site (0.17 eV calculated for H$_2$ on pristine Pd (111) without NH$_3$). Note that the dissociation on the Pd$_3$Ag-terminated Pd$_3$Ag(111) surface shows a secondary reaction step that corresponds mainly to surface diffusion, however, with no significant energy barrier compared to the primary reaction step corresponding to physisorption of H$_2$ on a bridge site.

The vibrational frequencies of hydrogen for the initial, precursor, transition, and final states without pre-adsorbed NH$_3$ and with pre-adsorbed NH$_3$ following path (2) for the three surfaces are summarized in Table 2. All precursor states, except for pristine Pd(111), show a single vibrationally unstable phonon mode, apparent from the calculated imaginary frequencies in parenthesis. The precursor state for pristine Pd(111) shows no imaginary frequency and is a true metastable phase. The vibrational properties for the precursor state without NH$_3$ is also obtained from isolated geometry optimized structures, confirming that this is not an artifact from the structures obtained by the ci-NEB calculations, but rather an inherent behavior of the precursor configurations investigated. All transition states show 1–3 vibrationally unstable phonons, confirming their instability.

3.4. Surface segregation

The H$_2$ flux inhibition level during continuous exposure to NH$_3$ is also shown experimentally to change over time [16]. As discussed by Svenum et al. [26], the surface termination, and hence the hydrogen permeability, can largely be influenced by adsorption induced surface segregation since the surfaces are likely to equilibrate over time under experimentally relevant conditions [38]. To address this, surface segregation effects for Pd$_3$Ag with varying NH$_3$ and H coverages have been investigated.

Following the work in Ref. [26], seven different Pd$_3$Ag surfaces have been investigated, illustrated in Fig. 10. The labeling refers to the number of Ag atoms in each of the seven atomic layers (four atoms per layer in total), counted from the top surface - where the adsorption occurs - to the bottom surface. The Pd$_3$Ag-terminated Pd$_3$Ag(111) surface investigated above corresponds to the Pd$_3$Ag-1111111 configuration, while the Pd-terminated Pd$_3$Ag(111) surface corresponds to the Pd$_3$Ag-0211111 configuration.

The relative energies for the different configurations in Fig. 10 as a function of hydrogen coverage are shown in Fig. 11(a). Ag-rich surfaces
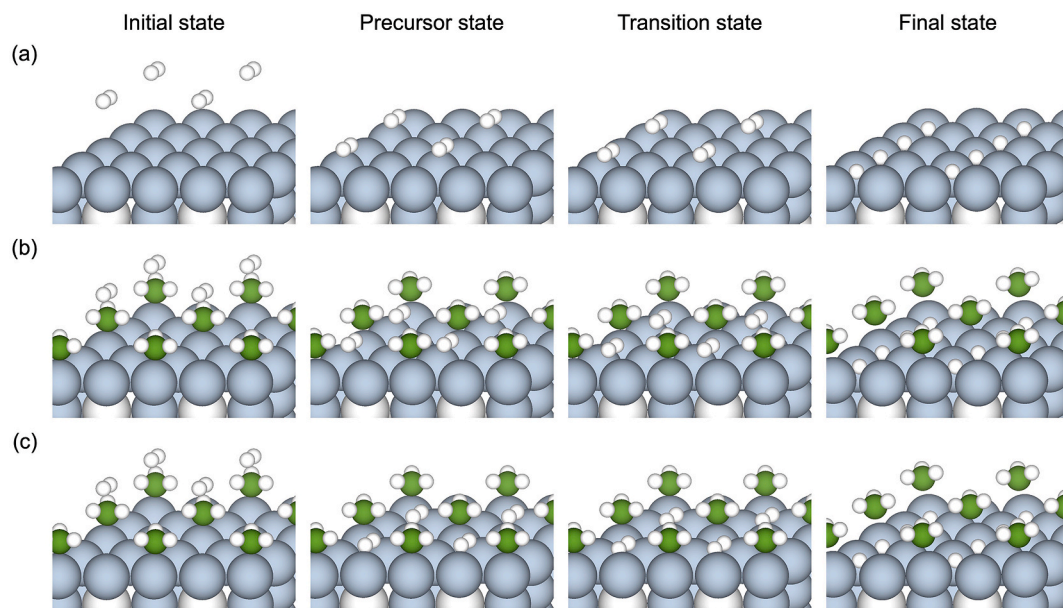
Fig. 9. Calculated crystal structures for the initial, precursor, transition, and final states during hydrogen dissociation on Pd-terminated Pd$_3$Ag(111) (a) without and (b, c) with NH$_3$ pre-adsorbed on the surface ($\theta_{NH3} = 1/4$) for (b) path (1) and (c) path (2). Comparable dissociation paths are found for the other surfaces investigated.

Table 2
Calculated vibrational frequencies of hydrogen along the dissociation paths with and without NH$_3$ pre-adsorbed on the surfaces in Figs. 8 and 9. The values marked with "i" in parenthesis are vibrationally unstable phonons with an imaginary frequency.

State	ν_i (cm^{-1})	
	$\theta_{NH3} = 0$	$\theta_{NH3} = 1/4$
Pd(111)		
Initial	4327	4330
Precursor	2667, 1540, 795, 212, 155, 130	1598, 1160, 518, 454, 329 (i347)
Transition	1901, 1889, 111 (i271, i409, i535)	1553, 1418, 202 (i134, i384, i491)
Final	1001, 983, 876, 870, 844, 825	1119, 1108, 987, 940, 792, 701
Pd$_3$Ag-terminated Pd$_3$Ag(111)		
Initial	4326	4326
Precursor	2870, 1366, 763, 227, 198 (i108)	1356, 1346, 852, 412, 342 (i421)
Transition	1573, 1478, 270, 239 (i217, i777)	1841, 1815, 329, 320, 127 (i252)
Final	1084, 1071, 1069, 1030, 627, 527	1353, 1329, 939, 863, 573, 465
Pd-terminated Pd$_3$Ag(111)		
Initial	4326	4326
Precursor	2884, 1348, 714, 220, 181 (i103)	1826, 1084, 549, 381, 243 (i335)
Transition	2388, 1529, 790, 142 (i170, i228)	1329, 1150, 712 (i189, i374, i377)
Final	960, 920, 889, 868, 856, 836	1114, 1098, 1003, 949, 796, 721

are preferred at lower θ_H, while Pd-rich surfaces are preferred at higher θ_H. For the saturation coverage $\theta_{H,sat} = 1$, the Pd$_3$Ag-0211111 configuration is the most favored, in line with previous DFT work [26]. This suggest that in pure hydrogen, the surface is expected to be terminated mainly by Pd, which is also confirmed experimentally [39].

Fig. 11(b) shows the relative energies as a function of θ_{NH3} up to the saturation coverage $\theta_{NH3,sat} = 1/4$. For the coverages investigated, Ag-rich surfaces are preferred. A small trend for preference towards higher Pd-content at the surface with increasing θ_{NH3} is observed, however, less pronounced than for the changes with θ_H in Fig. 11(a). This suggests that in pure NH$_3$, the surface is expected to be terminated mainly by Ag.

The segregation effect for co-adsorption of hydrogen and NH$_3$ with $\theta_{NH3} = 1/4$ is shown in Fig. 11(c). Comparable to the pure hydrogen case in Fig. 11(a), the surface is expected to be Ag-rich at lower θ_H, and Pd-

rich at higher θ_H. No significant differences between the energy profiles with and without NH$_3$ present in Fig. 11(c) and (a), respectively, are observed, suggesting that any segregation effects are governed mostly by the surface coverage of hydrogen. Since the hydrogen saturation coverage is expected to reduce in the presence of NH$_3$ on the surface (Fig. 7), and reducing the hydrogen coverage promotes Ag-rich surfaces (Fig. 11(a)), segregation of Ag towards the surface during operation over time could occur. This is confirmed by the co-adsorption energetics in Fig. 11(c), where the configurations 2011111 to 0031111 differ only by ~0.1 eV in energy when assuming a hydrogen saturation coverage of $\theta_{H,sat} = 1/2$ in the presence of NH$_3$ as described above.

4. Conclusion

In this study, the adsorbate-adsorbate interactions during co-adsorption, the influence the presence of NH$_3$ has on the hydrogen dissociation kinetics, and surface segregation effects on Pd(111) and Pd$_3$Ag(111) surfaces in the presence of NH$_3$ and/or hydrogen have been investigated in detail using DFT calculations.

The initial adsorbate thermodynamical modelling with isolated adsorbates showed a competitive adsorption between hydrogen and NH$_3$. The NH$_3$ coverage were found to increase on the expense of the hydrogen coverage at lower p_{NH3}/p_{H2} with decreasing temperature, in agreement with experimental observations that the H$_2$ flux inhibition becomes more pronounced at lower temperatures. For finite adsorbate concentrations, including significant adsorbate-adsorbate interactions, the saturation coverage of hydrogen at relevant operating conditions (673 K) was found to be $\theta_{H,sat} = 1$ for the Pd-terminated surfaces investigated, and $\theta_{H,sat} = 3/4$ for the Pd$_3$Ag-terminated surface, while the saturation coverage of NH$_3$ was found to be $\theta_{NH3,sat} = 1/4$ for all surfaces. With $\theta_{NH3} = 1/4$ pre-adsorbed on the surface, the hydrogen adsorption was significantly weakened, with a destabilization energy in the order of ~0.2 eV and a reduced hydrogen saturation coverage of $\theta_{H,sat} = 1/2$.

The hydrogen dissociation was found to be a non-activated process on the clean surfaces, characterized by no energy barrier in the calculated minimum energy path. Upon pre-adsorption of NH$_3$, the dissociation becomes activated with an energy barrier in the order of ~0.2 eV. The dissociation mechanism was also found to change with NH$_3$ present on the surface.
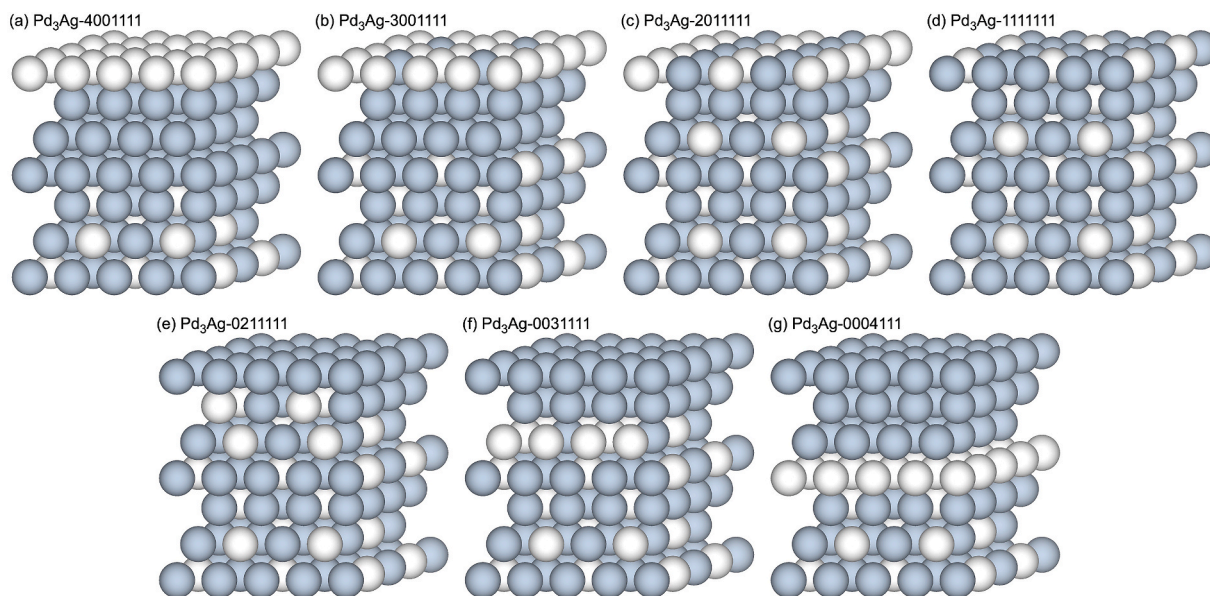
Fig. 10. The supercells used to model surface segregation as a function of surface coverage. The numbers refer to the number of Ag-atoms per atomic layer (four atoms per layer in total), counting from the top to the bottom surfaces. The adsorption occurs on the top surface layer.
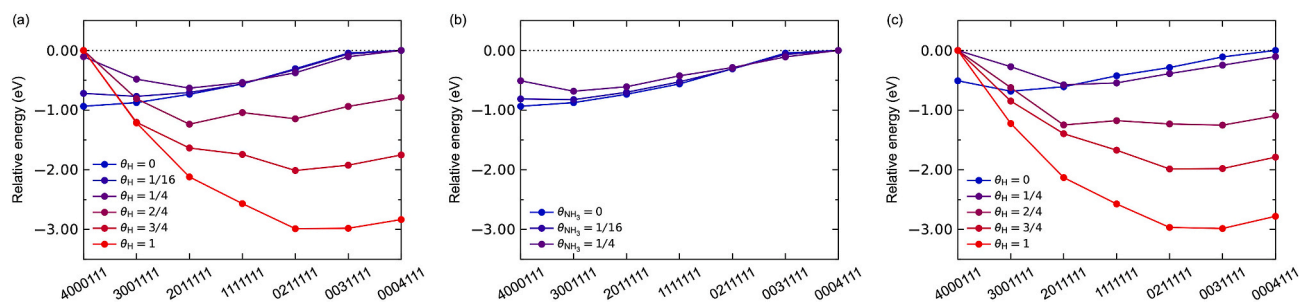

Fig. 11. Calculated relative energies for the different configurations in Fig. 10 as a function of surface coverage for adsorption of (a) hydrogen, (b) NH$_3$, and (c) co-adsorption of hydrogen and NH$_3$ with varying θ_H and a constant $\theta_{NH3} = 1/4$.

The Pd$_3$Ag(111) surface was found to be Ag-rich in lower θ_H, and Pd-rich at higher θ_H. A similar trend was also observed for adsorption with NH$_3$. The co-adsorption with varying θ_H and constant $\theta_{NH3} = 1/4$ suggest that any segregation effect is governed mainly by the hydrogen surface coverage, where the presence of NH$_3$ on the surface could promote segregation of Ag towards the surface due to the associated reduction in the hydrogen surface coverage during co-adsorption.

These results suggest that both the hydrogen surface coverage and dissociation kinetics are hindered by the presence of NH$_3$ on the surface. Furthermore, our calculations indicate possible segregation of Ag towards the surface in the presence of NH$_3$. This could explain the measured long-term H$_2$ flux inhibition in NH$_3$.

CRediT authorship contribution statement

Didrik R. Småbråten: Conceptualization, Data curation, Investigation, Writing – original draft, Writing – review & editing. **Marie D. Strømsheim:** Conceptualization, Funding acquisition, Methodology, Project administration, Writing – review & editing. **Thijs Peters:** Conceptualization, Funding acquisition, Methodology, Project administration, Resources, Writing – original draft, Writing – review & editing.

Declaration of competing interest

The authors declare that they have no known competing financial interests or personal relationships that could have appeared to influence

the work reported in this paper.

References

[1] Kurien C, Mittal M. Utilization of green ammonia as a hydrogen energy carrier for decarbonization in spark ignition engines. Int J Hydrogen Energy 2023;48:28803.

[2] Langella G, de Joannon M, Sabia P, Iodice P, Amoresano A. Ammonia as a fuel for internal combustion engines: latest advances and future challenges. J. Phys. Conf. Ser. 2022;2385:012036.

[3] Qi Y, Liu W, Liu S, Wang W, Peng Y, Wang Z. A review on ammonia-hydrogen fueled internal combustion engines. ETransportation 2023;18:100288.

[4] Tornatore C, Marchitto L, Sabia P, De Joannon M. Ammonia as green fuel in internal combustion engines: state-of-the-art and future perspectives. Front Mech Eng 2022;8.

[5] Valera-Medina A, Amer-Hatem F, Azad AK, Dedoussi IC, de Joannon M, Fernandes RX, Glarborg P, Hashemi H, He X, Mashruk S, McGowan J, Mounaim-Rouselle C, Ortiz-Prado A, Ortiz-Valera A, Rossetti I, Shu B, Yehia M, Xiao H,

Costa M. Review on ammonia as a potential fuel: from synthesis to economics. Energy Fuels 2021;35:6964.

[6] Rathore SS, Biswas S, Fini D, Kulkarni AP, Giddey S. Direct ammonia solid-oxide fuel cells: a review of progress and prospects. Int J Hydrogen Energy 2021;46: 35365.

[7] Dhawale DS, Biswas S, Kaur G, Giddey S. Challenges and advancement in direct ammonia solid oxide fuel cells: a review. Inorg Chem Front 2023;10:6176.

[8] Cheliotis M, Boulougouris E, Trivyza NL, Theotokatos G, Livanos G, Mantalos G, Stubos A, Stamatakis E, Venetsanos A. Review on the safe use of ammonia fuel cells in the maritime industry. Energies 2021;14:3023.

[9] Halseid R, Vie PJS, Tunold R. Effect of ammonia on the performance of polymer electrolyte membrane fuel cells. J Power Sources 2006;154:343.

[10] García-García FR, Ma YH, Rodríguez-Ramos I, Guerrero-Ruiz A. High purity hydrogen production by low temperature catalytic ammonia decomposition in a multifunctional membrane reactor. Catal Commun 2008;9:482.

[11] Collins JP, Way JD. Catalytic decomposition of ammonia in a membrane reactor. J Membr Sci 1994;96:259.

[12] Itoh N, Oshima A, Suga E, Sato T. Kinetic enhancement of ammonia decomposition as a chemical hydrogen carrier in palladium membrane reactor. Catal Today 2014; 236:70.

[13] Cechetto V, Di Felice L, Medrano JA, Makhloufi C, Zuniga J, Gallucci F. H_2 Production via ammonia Decomposition in a catalytic membrane reactor. Fuel Process Technol 2021;216:106772.

[14] Cechetto V, Agnolin S, Di Felice L, Pacheco Tanaka A, Llosa Tanco M, Gallucci F. Metallic supported Pd-Ag Membranes for simultaneous ammonia Decomposition and H_2 Separation in a membrane reactor: experimental Proof of concept. Catalysts 2023;13:920.

[15] Zhang J, Xu H, Li W. High-purity CO_x-free H_2 Generation from NH_3 via the ultra Permeable and highly selective Pd membranes. J Membr Sci 2006;277:85.

[16] Peters TA, Polfus JM, Stange M, Veenstra P, Nijmeijer A, Bredesen R. H_2 flux Inhibition and Stability of Pd-Ag Membranes under Exposure to trace Amounts of NH_3. Fuel Process Technol 2016;152:259.

[17] Zhang Z, Liguori S, Fuerst TF, Way JD, Wolden CA. Efficient ammonia decomposition in a catalytic membrane reactor to enable hydrogen storage and utilization. ACS Sustainable Chem Eng 2019;7:5975.

[18] Cechetto V, Di Felice L, Gallucci F. Advances and Perspectives of H_2 Production from NH_3 Decomposition in membrane reactors. Energy Fuels 2023;37:10775.

[19] Clark D, Malerød-Fjeld H, Budd M, Yuste-Tirados I, Beeaff D, Aamodt S, Nguyen K, Ansaloni L, Peters T, Vestre PK, Pappas DK, Valls MI, Remiro-Buenamañana S, Norby T, Bjørheim TS, Serra JM, Kjølseth C. Single-step hydrogen Production from NH_3 , CH_4 , and Biogas in stacked proton ceramic reactors. Science 2022;376:390.

[20] Peters TA, Polfus JM, van Berkel FPF, Bredesen R. Interplay between Propylene and H_2S Co-Adsorption on the H_2 flux Characteristics of Pd-alloy membranes Employed in propane dehydrogenation (PDH) processes. Chem Eng J 2016;304: 134.

[21] Jiang Z, Pan Q, Li M, Yan T, Fang T. Density functional theory study on direct catalytic decomposition of ammonia on Pd(111) surface. Appl Surf Sci 2014;292: 494.

[22] Herron JA, Tonelli S, Mavrikakis M. Atomic and molecular adsorption on Pd(111). Surf Sci 2012;606:1670.

[23] Stolbov S, Rahman TS. First-principles study of some factors controlling the rate of ammonia decomposition on Ni and Pd surfaces. J Chem Phys 2005;123.

[24] Novell-Leruth G, Valcárcel A, Pérez-Ramírez J, Ricart JM. Ammonia Dehydrogenation over platinum-group metal surfaces. Structure, stability, and Reactivity of adsorbed NH_x species. J Phys Chem C 2007;111:860.

[25] Svenum I-H, Herron JA, Mavrikakis M, Venvik HJ. $Pd_3Ag(111)$ as a model System for hydrogen separation membranes: combined Effects of CO Adsorption and surface Termination on the Activation of molecular hydrogen. Top Catal 2020;63: 750.

[26] Svenum I-H, Herron JA, Mavrikakis M, Venvik HJ. Adsorbate-induced Segregation in a PdAg membrane model system: $Pd_3Ag(111)$. Catal Today 2012;193:111.

[27] Blöchl PE. Projector augmented-wave method. Phys Rev B 1994;50:17953.

[28] Kresse G, Furthmüller J. Efficient iterative Schemes for ab initio total-energy calculations Using a plane-wave basis set. Phys Rev B 1996;54:11169.

[29] Kresse G, Joubert D. From ultrasoft pseudopotentials to the projector augmented-wave method. Phys Rev B 1999;59:1758.

[30] Perdew JP, Burke K, Ernzerhof M. Generalized gradient approximation made simple. Phys Rev Lett 1996;77:3865.

[31] Henkelman G, Uberuaga BP, Jónsson H. A climbing image nudged elastic band method for finding saddle points and minimum energy paths. J Chem Phys 2000; 113:9901.

[32] Henkelman G, Jónsson H. Improved tangent estimate in the nudged elastic band method for finding minimum energy paths and saddle points. J Chem Phys 2000; 113:9978.

[33] M. Chase, NIST-JANAF thermochemical tables, fourth ed..

[34] Campbell CT, Sellers JRV. The entropies of adsorbed molecules. J Am Chem Soc 2012;134:18109.

[35] Polfus JM, Peters T, Bredesen R, Løvvik OM. Vacancy diffusion in palladium hydrides. Phys Chem Chem Phys 2021;23:13680.

[36] Dong W, Hafner J. H_2 dissociative Adsorption on Pd(111). Phys Rev B 1997;56: 15396.

[37] Dipojono HK, Padama AAB, Ozawa N, Nakanishi H, Kasai H. A first principles Study on Dissociation and adsorption Processes of H_2 on Pd_3 Ag(111) surface. Jpn J Appl Phys 2010;49:115702.

[38] Greeley J, Mavrikakis M. Alloy catalysts designed from first principles. Nat Mater 2004;3:810.

[39] Shu J, Bongondo BEW, Grandjean BPA, Adnot A, Kaliaguine S. Surface segregation of Pd-Ag membranes upon hydrogen permeation. Surf Sci 1993;291:129.